

Vortices and Dust Devils As Observed by the MEDA Instruments onboard Mars 2020 Perseverance Rover

BRIAN JACKSON¹

¹*Department of Physics
Boise State University*

1910 University Drive, Boise ID 83725-1570 USA

ABSTRACT

An important and perhaps dominant source of dust in the martian atmosphere, dust devils play a key role in Mars' climate. Datasets from previous landed missions have revealed dust devil activity, constrained their structures, and elucidated their dust-lifting capacities. However, each landing site and observational season exhibits unique meteorological properties that shape dust devil activity and help illuminate their dependence on ambient conditions. The recent release of data from the Mars Environmental Dynamics Analyzer (MEDA) instrument suite onboard the Mars 2020 Perseverance rover promises a new treasure-trove for dust devil studies. In this study, we sift the time-series from MEDA's Pressure Sensor (PS) and Radiative and Dust Sensors (RDS) to look for the signals of passing vortices and dust devils. We detected 309 vortex encounters over the mission's first 89 sols. Consistent with predictions, these encounter rates exceed InSight and Curiosity's encounter rates by factors of several. The RDS time-series also allows us to assess whether a passing vortex is likely to be dusty (and therefore is a true dust devil) or dustless. We find that about one-third of vortices show signs of dust-lofting, although unfavorable encounter geometries may have prevented us from detecting dust for other vortices. In addition to these results, we discuss prospects for vortex studies as additional data from Mars 2020 are processed and made available.

Keywords: Planetary atmospheres (1244), Mars (1007)

1. INTRODUCTION

The Mars 2020 Perseverance rover landed on 2021 February 18 ($L_s = 5.6^\circ$ – <http://www.tinyurl.com/MarsClock>) at the Octavia E. Butler Landing site within Jezero Crater on Mars (18.4447° N, 77.4508° E). The primary goals of the mission are to seek signs of extant and extinct life and collect rock and soil samples for a future return to Earth by acquiring imaging, spectroscopy, and other measurements to characterize Martian soils, rocks, atmosphere, and other aspects of the environment (Farley et al. 2020). To address these goals, the rover carries seven scientific instruments, as well as a sample acquisition and caching system.

These instruments include the Mars Environmental Dynamics Analyzer (MEDA) suite consisting of sensors to measure environmental variables – air pressure and temperature (the pressure and temperature sensors, PS and ATS respectively), up/downward-welling radiation and dust optical depth (via the Radiation and Dust Sensor RDS), wind speed and direction (wind sensors 1 and 2, WS1 and 2), relative humidity (via the humidity sensor HS), and ground temperature (via the Thermal Infrared Sensor TIRS). This combination of powerful, accurate, and precise instrumentation will enable novel investigations of atmospheric processes on Mars, ranging from estimation of the near-surface radiation budget on sub-diurnal and longer timescales to exploration of the role of dust in thermal forcing to investigation of the wind stress thresholds for driving aeolian transport (Rodriguez-Manfredi et al. 2021).

Small-scale, dry, and dust-laden convective vortices, dust devils act as a key if ephemeral aeolian transport mechanism on the surface of Mars, lofting perhaps as much or more dust than any other mechanism on Mars (Fenton et al. 2016). Observations of martian dust devils go back to the Viking mission (Thomas & Gierasch 1985; Ringrose et al. 2003), and they appear frequently in imagery from landed and orbiting spacecraft (Murphy et al. 2016; Fenton & Lorenz 2015). As a boundary layer phenomenon, they also register in meteorological datasets collected both on Mars and the Earth. These signals come in the form of short-lived (few to tens of seconds), negative pressure excursions ($\Delta P \lesssim 1\%$

of the ambient pressure), accompanied by rapid changes in wind speed and direction (Kahanpää & Viúdez-Moreiras 2021).

However, pressure and wind excursions do not suffice to distinguish dust devils, which are vortices carrying dust, from dustless vortices, which are governed by the same physics (Steakley & Murphy 2016). Indeed, the precise conditions that allow a dustless vortex to become a dust devil are not clear but likely depend on the availability of dust and the vortex wind speeds. Instrumentation measuring solar insolation, alongside pressure and winds, can be used to determine whether a passing vortex is dust-laden or not: a dusty vortex can register either a dip in insolation (if the dust devil’s shadow passes over the sensor) or a spike (if the dust scatters insolation into the sensor). In either case, the measured insolation excursion relates directly to the dust devil’s optical depth τ (in the limit of small τ). Lorenz & Jackson (2015) deployed such an instrument suite on a terrestrial playa and found 20% of events caused dimming greater than about 2%. The encounters without detected attenuation may either be dustless vortices or the encounter geometry simply did not produce a signal. Stronger dimming was associated with larger pressure drops, presumably more vigorous and therefore windier vortices. Understanding the relationships between a vortex’s pressure and wind profiles and its dust content is critical for accurately estimating the contribution of dust devils to the martian atmospheric dust budget, key to Mars’ climate (Basu et al. 2004).

The initial release of data from Mars 2020’s MEDA PS (pressure) and RDS (radiation and dust) instrument provide an opportunity to explore these relationships in a novel locale on Mars. Moreover, since vortex formation depends on ambient meteorological conditions (Rafkin et al. 2016), assessment of their occurrence rate provides a probe of Mars’ boundary layer. Fortunately, Newman et al. (2021) recently conducted a comprehensive survey of model predictions for the meteorology within Jezero Crater and observed by Perseverance. That study included predictions of vortex occurrence and suggested that vortices may occur more frequently within Jezero than at other sites hosting recently landed Mars missions, including the InSight mission (Spiga et al. 2021) and the Mars Science Laboratory (MSL) Curiosity rover (Kahanpää & Viúdez-Moreiras 2021).

In this study, we analyze the MEDA data from the Mars 2020 Perseverance mission released on 2021 Aug 20 to assess the rates of vortex and dust devil occurrence. Over the 89 sols of currently available mission data, we estimate Mars 2020 encountered at least 309 vortices, one-third of which induced statistically significant excursions in insolation as observed by RDS. Unfortunately, this same data release did not include fully processed wind data from MEDA WS, and so an analysis of winds associated with these encounters must await future studies. We also leave the cache of images collected by Mastcam-Z and Perseverance’s engineering cameras for future analysis. Our preliminary assessment, however, does comport with meteorological predictions: Jezero Crater seems to be significantly more active than the InSight landing site or Gale Crater, as Mars 2020 encountered nearly 5 vortices per sol.

2. DATA AND MODEL ANALYSIS

2.1. Pressure Sensor Data Analysis and Modeling

The analysis presented here follows closely the process employed in Jackson et al. (2021). For the present study, we analyzed pressure time-series from the PS instrument available from NASA PDS (https://pds-atmospheres.nmsu.edu/PDS/data/PDS4/Mars2020/mars2020_meda/). We used the data set labeled “data_derived.env” since it represents the most completely processed and calibrated data set (see the Mars 2020 MEDA PDS Archive Bundle Software Interface Specification for details – https://pds-atmospheres.nmsu.edu/PDS/data/PDS4/Mars2020/mars2020_meda/document/meda_bundle.sis.pdf). The data are divided up by mission sol and typically span from midnight one sol to midnight the next, with a sampling rate of 1 Hz; however, the data for all sols include gaps of at least an hour or more. Some sols (early in the mission) span only a few hours, sols 1, 2, 4, 9, 14, 19, and 22. Sol 10 does not seem to have a pressure time-series at all. Thus, we excluded all these sols from our analysis. Figure 1(a) shows a representative raw pressure time-series from sol 82 of the mission.

We model the pressure signal of a vortex, dustless or dusty, as in Jackson et al. (2021):

$$\Delta P(t) = \frac{-\Delta P_0}{1 + \left(\frac{t-t_0}{\Gamma/2}\right)^2} \quad (1)$$

where t is the time, t_0 is the time of closest approach, ΔP_0 is the excursion amplitude, and Γ is the observed profile full-width/half-max (FWHM). The PS pressure time-series exhibit a variety of variations on timescales of hours to days, related to meteorological phenomena other than vortices (cf. Pla-García et al. 2020; Newman et al. 2021). These

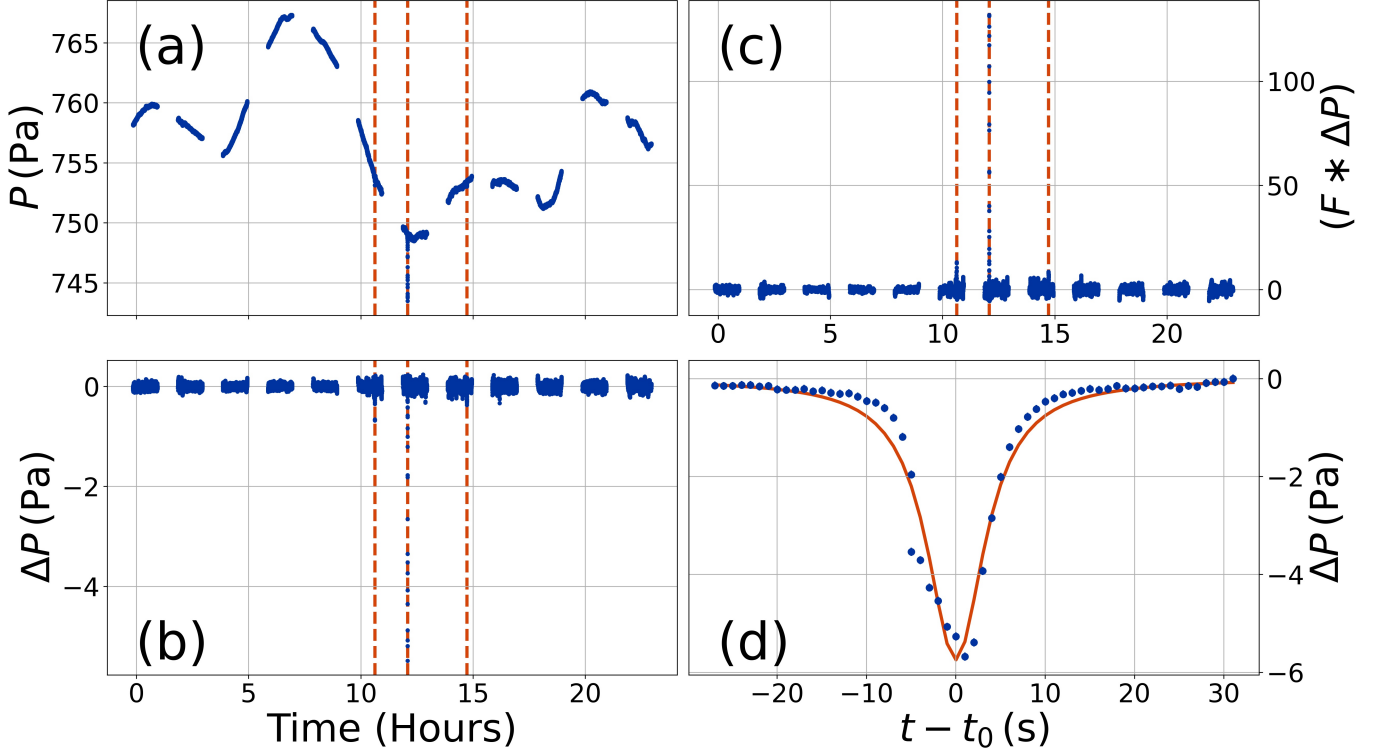


Figure 1. (a) The pressure time-series for sol 82, as blue dots. The vertical orange lines highlight the detected vortex signals. (b) The time-series after application of the mean boxcar filter. Apparent by eye, the scatter $\sigma_{\Delta P}$ in the time-series increases around mid-day. (c) Convolution of the matched filter with the time-series in (b). (d) A model fit (solid orange line) to the deepest vortex discovered on sol 82. Uncertainties are shown but are barely larger than the point diameters.

other signals obscure the short-lived vortex signals, and so we applied a high-pass boxcar filter to the raw pressure data with a window size of 500s to suppress the long-term variability. Experimentation with the data showed this window size provided a reasonable balance between flattening the long-term signals without significantly distorting the vortex signals. The resulting detrended pressure time-series exhibit standard deviations $\sigma_{\Delta P}$ between 0.05 and 0.08 Pa. Figure 1(b) shows the detrended dataset for sol 82.

To recover the vortex signals, we then applied a matched filter with a shape given by Equation 1 to the detrended data. In other words, we marched a Lorentzian profile, point-by-point, across the time series, convolving it with the time-series, producing a convolution signal $F * \Delta P$. We then subtracted the mean value of the resulting convolution signal and divided by the standard deviation to scale the spectrum by the intrinsic noise in the dataset. When a short-lived, negative pressure excursion occurs in the time-series, the convolution signal shows large positive spike. Experimentation with the data suggested a threshold value of $F * \Delta P \geq 7$ provides a good balance between excluding spurious or doubtful excursions and recovering statistically significant excursions. Figure 1(c) shows the convolution signal for the data in panel (b). Vertical, dashed orange lines show the spikes exceeding our detection threshold.

Finally, using the Levenberg-Marquardt algorithm (cf. Press et al. 2007), we fit each putative vortex signal from each sol’s data to retrieve best-fit t_0 , ΔP_0 , and Γ -values. To avoid signal distortion from our detrending process, we fit the original, un-detrended data (Figure 1a), which required us also to add a background linear trend to the vortex signal itself. We used the standard deviation for each sol’s detrended pressure time-series as the per-point uncertainties. Uncertainties on model parameters are given by the square root of the variable covariance matrix, scaled by the square root of the reduced χ^2 -value for the model fit, effectively imposing $\chi^2 = 1$ (Press et al. 2007). Figure 1(d) shows the deepest vortex we detected, with $\Delta P_0 = (5.7 \pm 0.9)$ Pa and $\Gamma = (7.2 \pm 2.4)$ s.

2.2. Radiation and Dust Sensor Data Analysis and Modeling

We also conducted a preliminary analysis of the RDS radiometric time-series. As described in Rodriguez-Manfredi et al. (2021), the RDS suite includes 16 independent sensors designed to measure (or to help calibrate the measurements

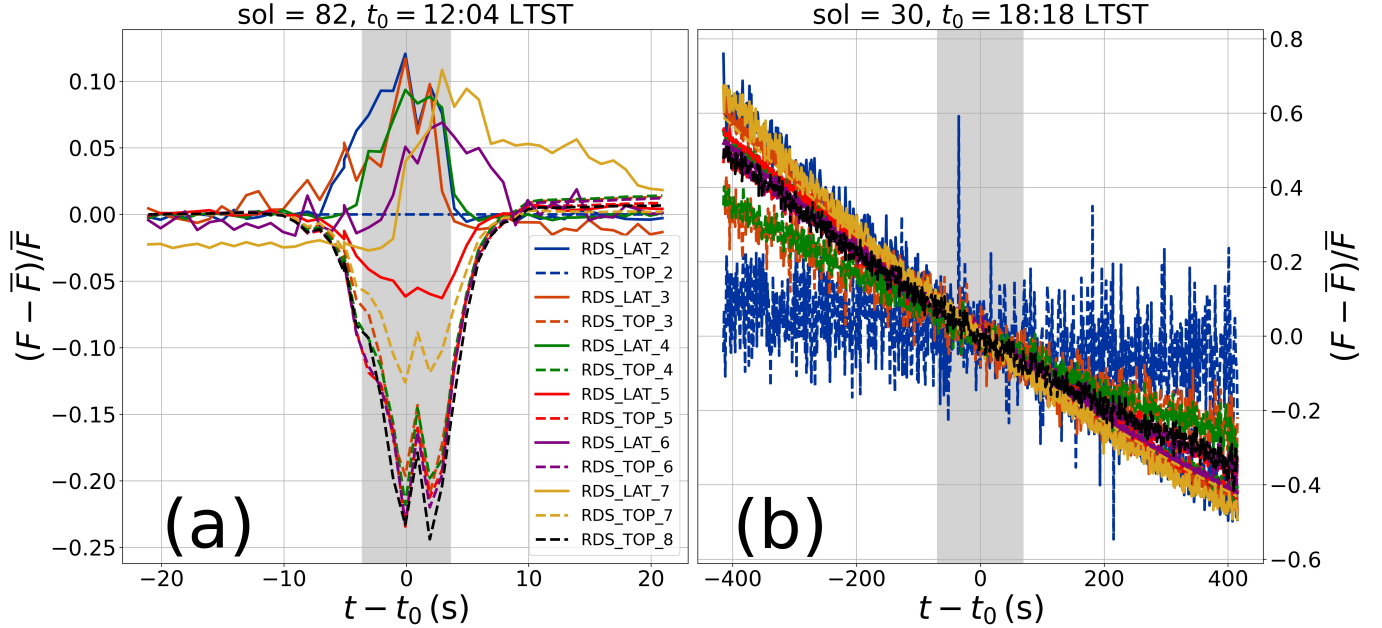


Figure 2. (a) RDS time-series collected during the vortex encounter on sol 82 at $t_0 = 12:04$ LTST. Each combination of line color and styles reflects a specific sensor as indicated in the legend. The filled grey band shows the FWHM (Γ) for the vortex encounter. (b) The same as in (a), except for an encounter on sol 30 at $t_0 = 18:18$ LTST, showing no statistically significant excursion.

of) the upward and downward-welling radiation. The discrete photodetectors, numbered 1 through 8, are arrayed in a circle on the RDS assembly, some on top and pointed up at the sky (“TOP”) and others pointed outward from the assembly laterally (“LAT”). The eight LAT sensors all sample a narrow band of wavelengths 750 ± 10 nm, while the TOP sensors each sample different bands, spanning from 190 nm to 1100 nm. Sensor LAT_1 is blocked by the Sampling and Caching Subsystem (SCS), and so the mission has blinded it to assess the degradation of all the sensors due to radiation (Rodriguez-Manfredi et al. 2021). The detectors (except LAT_1) are sensitive to scattering of light by the martian dust. In the current data release, the RDS dataset has not been completely processed (i.e., the data are categorized as “calibrated” – https://pds-atmospheres.nmsu.edu/PDS/data/PDS4/Mars2020/mars2020_meda/document/meda_bundle-sis.pdf). In any case, the data, collected throughout most sols at 1-Hz sampling, are sufficiently processed for the preliminary analysis presented here.

The passage of a dust-laden vortex near the RDS sensors registers in the time-series as a series of (negative) dips and (positive) blips, as the dust scatters light into and away from the sensors (Lorenz & Jackson 2015). The structures of these signals may be complicated, reflecting the potentially complex column density structure within the vortices – Figure 2 provides examples during two vortex encounters, showing data from all the RDS sensors (except LAT_1).

In the optically thin limit, the magnitude of the excursion (positive or negative) scales with column optical depth, so we consider the maximum excursion during an encounter from among all the sensors as measured relative to the signal 3Γ before and after the time of encounter t_0 . We estimate the median value of the RDS signals \bar{F} and the scatter σ_F from these before and after periods. If the maximum of the absolute value of signal during the encounter exceeds $3\sigma_F$, we recorded this value $\max|\frac{F - \bar{F}}{\bar{F}}|$ as a statistically significant excursion. Other encounters were assigned a value of zero. (Because some of the resulting excursions appeared spurious, we filtered out values more than five standard deviations larger than the median value for all excursions.) No statistically significant excursion may represent either a dustless vortex or an encounter for which the light-scattering geometry simply did not produce an excursion (e.g., no shadow fell across the sensors).

3. RESULTS

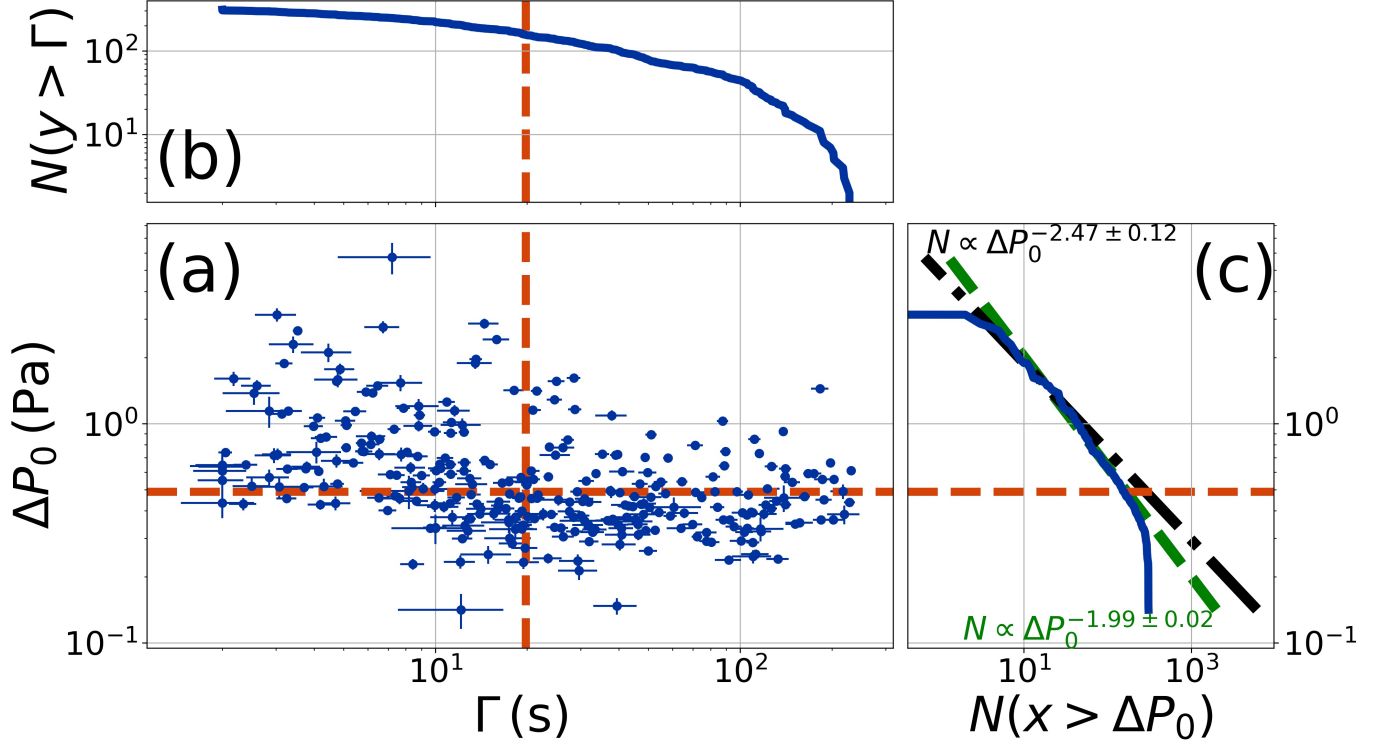


Figure 3. (a) The best-fit ΔP_0 - and Γ -values (blue dots) with error bars. (b) Cumulative histogram of Γ -values, along with the median value ($\Gamma_{\text{obs}} = (19.8 \pm 1.6)$ s) shown by the dashed, orange line. (c) Cumulative histogram of ΔP_0 -values, along with the median value ($\Delta P_{0\text{obs}} = (0.49 \pm 0.02)$ Pa) shown by the dashed, orange line. The dashed green line shows a power-law fit to the histogram for $\Delta P_0 > 0.5$ Pa with $N \propto \Delta P_0^{-1.99 \pm 0.02}$, while the dash-dotted black line shows a fit for $P_0 > 1.5$ Pa with $N \propto \Delta P_0^{-2.47 \pm 0.12}$.

Table 1. Vortex fit parameters.

Sol	t_0 (LTST)	ΔP_0 (Pa)	Γ (seconds)	$\max F - \bar{F} /\bar{F}$
15	16.3707 \pm 0.000114	0.984904 \pm 0.068435	12.2542 \pm 1.837820	-
15	16.314 \pm 0.000773	0.415701 \pm 0.044668	60.6367 \pm 13.816900	-
16	14.6367 \pm 0.000151	0.379955 \pm 0.013517	30.0529 \pm 1.997530	-
16	15.3834 \pm 0.000044	0.640507 \pm 0.089694	2.0 \pm 0.433102	-
16	12.7856 \pm 0.000208	0.386464 \pm 0.025529	22.5997 \pm 2.570970	0.00169065 \pm 0.000005
17	16.2986 \pm 0.000092	0.702297 \pm 0.010564	48.7334 \pm 1.587000	-
17	12.5356 \pm 0.000200	0.492874 \pm 0.085976	8.18257 \pm 2.533350	-
17	17.8581 \pm 0.000039	0.367957 \pm 0.007737	13.0428 \pm 0.536131	-
17	12.2736 \pm 0.000264	0.571312 \pm 0.014664	81.4562 \pm 4.438300	-
18	12.9773 \pm 0.000283	0.236445 \pm 0.016386	29.321 \pm 3.863790	-
18	17.1559 \pm 0.001036	0.331282 \pm 0.041331	116.587 \pm 22.191300	-
18	16.6598 \pm 0.000360	0.320163 \pm 0.010195	103.186 \pm 6.732560	-
18	11.0037 \pm 0.000096	0.423764 \pm 0.029448	9.95132 \pm 1.285670	-
18	13.0518 \pm 0.000091	0.386793 \pm 0.018292	13.9806 \pm 1.282720	-

Table 1 continued on next page

Table 1 (*continued*)

Sol	t_0 (LTST)	ΔP_0 (Pa)	Γ (seconds)	$\max F - \bar{F} /\bar{F}$
18	12.6796 \pm 0.000048	0.515416 \pm 0.057755	3.07285 \pm 0.580834	0.0092847 \pm 0.000008
18	16.7791 \pm 0.000204	0.366887 \pm 0.014552	38.1475 \pm 3.275710	-
18	12.8291 \pm 0.000312	0.385623 \pm 0.018000	48.1335 \pm 4.784080	-
18	15.4208 \pm 0.000094	0.718924 \pm 0.012809	38.9863 \pm 1.506310	-
20	12.241 \pm 0.000073	0.536808 \pm 0.016913	16.5358 \pm 1.074560	-
20	14.0927 \pm 0.000205	0.421187 \pm 0.015302	42.9868 \pm 3.394850	-
21	13.141 \pm 0.000031	3.1355 \pm 0.219155	3.02533 \pm 0.465361	0.00192864 \pm 0.000003
21	13.8778 \pm 0.000033	0.582045 \pm 0.018100	7.46973 \pm 0.471552	0.00999574 \pm 0.000010
21	15.0886 \pm 0.000152	0.373955 \pm 0.014049	28.4132 \pm 2.028530	-
21	11.2109 \pm 0.000218	0.364602 \pm 0.012416	45.4017 \pm 3.075540	-
21	13.5775 \pm 0.000168	0.460377 \pm 0.007473	74.7749 \pm 2.532200	-
28	12.3695 \pm 0.000022	1.48775 \pm 0.088153	2.59509 \pm 0.290522	-
28	14.2799 \pm 0.000023	0.857022 \pm 0.030365	4.20713 \pm 0.304774	-
28	14.3606 \pm 0.000259	0.41845 \pm 0.019684	44.4219 \pm 4.474780	-
28	12.1381 \pm 0.000051	0.5722 \pm 0.009182	23.4669 \pm 0.821994	0.00717381 \pm 0.000015
29	13.0917 \pm 0.000205	1.02549 \pm 0.020589	87.6513 \pm 3.720760	-
29	13.2853 \pm 0.000040	0.607585 \pm 0.075260	2.0 \pm 0.394681	-
29	16.6336 \pm 0.000130	0.330256 \pm 0.009634	32.7993 \pm 2.024730	-
30	18.3077 \pm 0.000188	0.922316 \pm 0.011631	138.481 \pm 3.515750	-
31	11.5649 \pm 0.000054	0.442776 \pm 0.020135	8.6582 \pm 0.811954	0.00261421 \pm 0.000003
31	11.4021 \pm 0.000198	0.233 \pm 0.016198	19.4375 \pm 2.410310	-
31	11.0237 \pm 0.000176	0.542184 \pm 0.012768	54.8825 \pm 2.780550	-
31	15.2366 \pm 0.000598	0.241091 \pm 0.010664	133.082 \pm 11.315600	-
32	11.8549 \pm 0.000090	0.385209 \pm 0.010507	24.0009 \pm 1.151680	-
32	11.5749 \pm 0.000154	0.719155 \pm 0.033137	24.7956 \pm 2.822760	0.0102962 \pm 0.000015
32	13.8621 \pm 0.000574	1.4434 \pm 0.064940	182.816 \pm 12.081100	-
32	13.866 \pm 0.000304	0.141472 \pm 0.025577	12.1285 \pm 4.585510	-
33	12.1815 \pm 0.000086	1.16113 \pm 0.026797	28.6962 \pm 1.448480	-
33	15.3253 \pm 0.000018	1.10825 \pm 0.044273	3.13237 \pm 0.243010	-
33	13.0402 \pm 0.000053	0.51586 \pm 0.045007	4.30737 \pm 0.653389	-
33	16.6325 \pm 0.000126	0.374217 \pm 0.029378	11.3671 \pm 1.751740	-
34	12.5034 \pm 0.000040	1.96397 \pm 0.042937	13.583 \pm 0.642782	0.00764198 \pm 0.000015
34	13.8024 \pm 0.000058	2.11022 \pm 0.206213	4.46191 \pm 0.844833	-
34	13.2047 \pm 0.000175	0.494111 \pm 0.016715	37.4652 \pm 2.598250	-
34	12.241 \pm 0.000085	0.502482 \pm 0.032056	9.94855 \pm 1.118020	-
34	15.5725 \pm 0.000031	0.42659 \pm 0.022386	4.19439 \pm 0.386226	-
34	12.4117 \pm 0.000242	0.425784 \pm 0.020002	41.9188 \pm 4.233850	-
34	13.5758 \pm 0.000021	0.511519 \pm 0.020685	3.71233 \pm 0.269258	-
34	11.8926 \pm 0.000165	0.54448 \pm 0.010653	64.4565 \pm 2.733770	-
34	12.3318 \pm 0.000017	1.0627 \pm 0.032077	4.09876 \pm 0.248018	-

Table 1 *continued on next page*

Table 1 (*continued*)

Sol	t_0 (LTST)	ΔP_0 (Pa)	Γ (seconds)	$\max F - \bar{F} /\bar{F}$
35	11.9202±0.000019	1.1395±0.047134	3.29337±0.255556	0.0036779±0.000003
35	12.0836±0.000191	0.32839±0.014190	33.3723±3.040980	-
35	14.2643±0.000177	0.289626±0.011096	31.9485±2.316740	-
36	10.2866±0.000092	1.20157±0.094171	8.82076±1.437670	-
36	12.7318±0.000038	1.48715±0.061834	6.46199±0.534053	-
36	12.1837±0.000335	0.394729±0.008735	108.612±4.988670	-
37	14.0538±0.000316	0.310993±0.017423	40.8732±4.904530	-
37	14.469±0.000047	0.585085±0.027885	7.10445±0.622337	0.00653669±0.000005
37	14.2297±0.000032	1.13689±0.048362	5.46122±0.476831	0.0347561±0.001702
37	12.1888±0.000026	1.17737±0.027714	7.85643±0.384723	-
38	12.5122±0.000367	0.425175±0.010518	121.19±6.409790	-
38	16.2626±0.000150	0.304873±0.012577	26.2693±2.177150	-
38	13.1623±0.000513	0.592514±0.018003	174.708±9.709780	0.00764625±0.000008
38	15.2973±0.000030	0.635877±0.036078	3.78208±0.405221	-
38	12.0754±0.000075	0.722829±0.009944	39.6168±1.170010	-
38	14.2174±0.000519	0.449871±0.013336	188.15±11.281200	0.0585171±0.000191
39	14.0523±0.000193	0.479192±0.011893	56.8503±2.998340	0.0819546±0.000008
39	12.4397±0.000086	0.417054±0.024081	10.6505±1.249030	-
39	14.7123±0.000169	0.448933±0.026475	25.2961±3.067770	-
39	14.7264±0.000078	0.723838±0.052178	7.7309±1.062420	0.029783±0.000009
39	12.1649±0.000020	1.60244±0.120255	2.17738±0.296138	-
39	11.0483±0.000045	1.25564±0.036872	10.9109±0.672565	-
41	15.9784±0.000136	0.324471±0.024970	12.7738±1.885260	0.00600243±0.000005
41	14.1436±0.000338	0.48928±0.031480	37.7349±4.838740	-
41	12.2339±0.000288	0.346825±0.012890	69.8497±5.192180	-
41	13.3274±0.000145	0.39799±0.015662	27.5177±2.313300	-
41	13.3039±0.000037	0.651998±0.014445	11.1883±0.511366	0.00914199±0.000008
41	11.6511±0.000098	0.544312±0.020736	17.4172±1.338050	-
44	14.8022±0.000547	0.540418±0.015163	148.02±8.994880	-
44	12.823±0.000079	0.842773±0.018641	27.1536±1.287480	-
44	15.7185±0.000022	0.653236±0.010182	10.3394±0.324616	-
44	13.8211±0.000063	0.624968±0.027504	10.4009±0.934193	0.0142526±0.000015
44	18.5894±0.000300	0.610232±0.008335	231.18±5.842730	-
44	10.8727±0.000076	0.298743±0.013227	12.2683±0.943523	0.0135891±0.000018
44	11.0415±0.000026	0.518657±0.043624	2.49673±0.333805	0.00310557±0.000002
45	12.9826±0.000097	0.529352±0.029339	13.2071±1.602310	0.0361472±0.000074
45	14.8746±0.000105	0.441599±0.011191	30.4257±1.615510	-
45	11.5547±0.000040	0.459288±0.019042	6.52864±0.557687	0.0234355±0.000008
45	10.8637±0.000106	0.484808±0.009809	40.3245±1.776050	0.00466019±0.000006
45	13.6082±0.000027	0.647297±0.076266	2.0±0.366998	-

Table 1 *continued on next page*

Table 1 (*continued*)

Sol	t_0 (LTST)	ΔP_0 (Pa)	Γ (seconds)	$\max F - \bar{F} /\bar{F}$
45	12.9656±0.000096	1.14464±0.068388	11.5473±1.407380	-
45	10.662±0.000063	0.455157±0.027258	7.62469±0.962837	0.00431803±0.000004
45	19.1922±0.000191	0.379174±0.009016	59.0076±2.978470	-
45	11.9529±0.000139	0.568621±0.028204	19.092±1.964270	0.00642702±0.000006
46	16.2435±0.000215	0.333582±0.051106	10.0035±2.821140	-
46	13.1785±0.000285	0.604119±0.029111	41.0418±3.888340	-
46	14.8121±0.000574	0.556657±0.018226	185.866±11.060200	0.00488161±0.000009
46	12.1617±0.000048	0.433228±0.031492	4.70512±0.556518	-
46	13.2073±0.000016	0.647835±0.031947	2.39047±0.213130	-
47	15.7173±0.000061	1.13926±0.184004	2.8504±0.797489	-
47	15.8798±0.000187	0.74621±0.015125	89.5566±3.589050	-
47	12.8197±0.000450	0.473547±0.015487	106.327±7.552660	0.00673164±0.000008
47	12.8101±0.000119	0.388373±0.024580	15.5413±2.078680	-
47	19.3469±0.000078	0.505048±0.030730	9.12177±1.038430	-
47	11.2173±0.000296	0.363668±0.011049	92.4425±5.552970	-
47	16.0525±0.000256	0.344189±0.020056	31.8055±3.654500	-
47	14.1712±0.000060	0.457718±0.010728	18.7992±0.924847	0.0170259±0.000013
47	12.4474±0.000166	0.242757±0.012578	23.4154±2.528000	0.00330866±0.000004
47	12.6544±0.000145	0.271034±0.014204	19.6879±1.934770	-
48	18.481±0.000367	0.465673±0.009123	162.656±6.638950	-
48	12.8843±0.001033	0.385115±0.037998	219.455±26.546400	-
48	15.3209±0.000506	0.392206±0.014427	101.754±8.032380	-
48	15.5267±0.000640	0.38645±0.020820	119.353±12.449600	-
49	15.5548±0.000090	0.457743±0.013723	21.5713±1.206170	-
49	12.5098±0.000019	0.848634±0.017537	6.55239±0.263532	-
49	15.4386±0.000294	0.360584±0.029057	30.8761±5.313310	-
49	13.31±0.000190	0.373482±0.012589	42.4045±3.056760	-
49	17.0127±0.000241	0.730289±0.011760	115.584±4.050970	-
50	11.3357±0.000149	0.329767±0.034977	18.2888±3.268160	-
50	11.8369±0.000030	1.09193±0.026363	8.86937±0.379784	-
50	15.3965±0.000026	1.39565±0.046535	5.91222±0.392865	-
50	16.5241±0.000129	0.890141±0.017401	51.0581±2.172450	-
50	13.5135±0.000046	0.676484±0.046939	4.74079±0.522683	-
50	11.3295±0.000242	0.795381±0.022403	71.1638±4.278090	-
50	11.5481±0.000047	0.608674±0.016372	12.4073±0.691337	0.0221572±0.000005
50	12.1811±0.000695	0.503822±0.022945	122.719±12.040100	-
50	11.414±0.000109	0.54655±0.014695	31.2715±1.842260	-
51	11.9099±0.000137	0.284097±0.015607	17.8646±1.730650	0.0168604±0.000023
51	12.2524±0.000060	0.741302±0.084224	4.07302±0.825464	-
52	15.869±0.000041	0.512999±0.017988	8.37922±0.595923	-

Table 1 *continued on next page*

Table 1 (*continued*)

Sol	t_0 (LTST)	ΔP_0 (Pa)	Γ (seconds)	$\max F - \bar{F} /\bar{F}$
52	13.1341±0.000123	0.369533±0.015367	21.1123±1.651650	0.0160222±0.000019
52	12.89±0.000045	0.477832±0.008693	17.5105±0.593793	-
52	13.3646±0.000028	0.434164±0.063562	2.0±0.538436	-
52	14.1261±0.000135	0.321689±0.010902	28.6868±1.822430	-
53	12.1819±0.000395	0.213683±0.020316	29.591±4.357770	-
53	11.0992±0.000022	0.429691±0.027895	2.34315±0.238466	-
53	15.0637±0.000219	0.346199±0.013746	39.8243±2.997840	-
53	11.9402±0.000709	0.36433±0.010236	184.109±11.041800	0.00406631±0.000008
53	12.9299±0.000055	0.459618±0.015396	11.7207±0.780240	0.0133582±0.000018
54	11.4914±0.000015	0.981791±0.021238	5.10925±0.222337	-
54	15.6098±0.000128	0.455556±0.020568	20.6964±1.951150	-
54	13.9745±0.000335	0.291722±0.011850	100.666±8.110730	0.0386044±0.000105
55	12.2396±0.000102	1.56017±0.046009	24.9438±1.579320	-
55	12.3726±0.000032	0.918791±0.021745	9.9355±0.483963	-
55	12.6411±0.000041	0.680566±0.013555	14.4932±0.575958	0.0189081±0.000012
55	14.5229±0.000172	0.488964±0.007482	82.6899±2.698900	-
55	12.4644±0.000276	0.48901±0.010263	97.6623±4.414280	-
55	12.8835±0.000335	0.287453±0.008691	80.4079±5.134010	-
55	15.3752±0.000111	0.464244±0.009094	44.9925±1.900780	0.0725133±0.000112
56	11.5384±0.000138	0.454519±0.015053	30.836±2.141040	-
56	13.2581±0.000120	0.331437±0.014077	19.1959±1.656360	-
56	10.3225±0.000022	0.454846±0.021892	3.25222±0.245984	-
56	14.6368±0.000056	0.52563±0.010618	19.9253±0.818422	-
56	13.4719±0.000087	0.608341±0.018135	20.6486±1.313690	-
56	12.0872±0.000017	0.815275±0.016967	5.71323±0.227667	-
56	14.9089±0.000071	0.977135±0.056234	8.8101±0.950328	-
56	12.5957±0.000087	1.53451±0.131571	7.68656±1.359740	0.00221409±0.000006
57	12.6475±0.000102	2.85409±0.148628	14.4607±1.638540	-
57	10.9753±0.000058	2.75132±0.171367	6.7326±0.880250	-
57	12.6981±0.000047	1.0122±0.029972	11.272±0.674619	-
58	16.3133±0.000072	0.432803±0.018605	11.1556±0.945098	-
59	15.6175±0.000201	0.643132±0.011908	88.6999±3.516070	-
59	12.2179±0.000103	0.334024±0.009313	25.8078±1.448600	0.00336156±0.000008
59	13.707±0.000296	0.333563±0.007488	105.602±5.109590	-
59	14.1325±0.000030	0.802795±0.027891	6.14302±0.412938	0.00589167±0.000004
59	12.9206±0.000099	0.489216±0.012025	29.201±1.496760	-
59	13.3063±0.000013	0.776581±0.014403	5.09216±0.190367	-
59	13.1248±0.000015	1.88305±0.063643	3.19165±0.207690	-
60	12.3266±0.000262	0.354428±0.037810	17.4198±3.296730	-
60	12.8781±0.000358	0.281339±0.017480	40.3129±5.147900	0.00749817±0.000007

Table 1 *continued on next page*

Table 1 (*continued*)

Sol	t_0 (LTST)	ΔP_0 (Pa)	Γ (seconds)	$\max F - \bar{F} /\bar{F}$
60	13.0153±0.000012	0.738513±0.023537	2.04689±0.103292	-
61	11.2643±0.000538	0.348511±0.012489	151.349±10.445100	-
61	14.899±0.000097	0.344936±0.012337	19.3875±1.361610	-
61	14.1009±0.000199	0.428758±0.012885	47.3475±2.914180	-
61	14.9829±0.000105	0.336884±0.010350	24.5937±1.450430	-
61	13.2419±0.000037	1.77198±0.104063	4.86715±0.550078	-
61	12.1926±0.000070	0.399513±0.010587	19.2122±1.017520	-
61	12.6621±0.000083	1.41987±0.050831	18.1096±1.387310	-
61	10.8831±0.000171	0.438991±0.019387	27.6039±2.460030	-
62	12.7562±0.000148	0.777029±0.031900	26.1917±2.332350	0.00203683±0.000005
62	12.5194±0.000026	0.723996±0.044564	3.03399±0.330736	0.0126539±0.000010
62	12.4537±0.000021	0.620157±0.028605	3.26894±0.265045	-
63	13.7303±0.000325	0.592277±0.009694	166.966±5.810300	-
63	15.8628±0.000096	0.463822±0.015792	18.8783±1.218360	-
63	11.8978±0.000382	0.556432±0.010646	203.151±7.233040	-
63	11.0335±0.000174	0.516402±0.013735	52.8185±3.047110	-
63	16.5082±0.000070	0.47503±0.018277	13.0995±0.973762	-
64	12.0514±0.000251	0.347589±0.013230	46.2432±3.491850	-
64	13.3725±0.000335	0.14728±0.012682	39.3738±6.376050	-
64	13.3687±0.000227	0.662817±0.007099	197.498±4.241130	-
64	12.3357±0.000085	1.28356±0.033493	24.5853±1.412680	-
64	12.8831±0.000086	1.15449±0.034846	20.8576±1.345420	0.058873±0.000013
64	12.9272±0.000122	0.364221±0.018659	17.3729±1.721580	-
65	11.1855±0.000021	0.973369±0.036876	3.9859±0.286788	-
65	12.9565±0.000040	1.37487±0.158458	2.54282±0.539094	0.0103284±0.000009
65	12.4928±0.000096	2.41823±0.109273	15.8879±1.581740	-
65	12.9374±0.000010	1.55766±0.023945	4.74225±0.144003	-
65	14.5896±0.000946	0.459085±0.063533	139.076±19.306300	-
65	13.6662±0.000144	0.342337±0.027012	12.4902±1.968290	0.080725±0.000020
65	15.2865±0.000090	0.472511±0.014208	21.7007±1.311430	-
65	12.3649±0.000026	0.621851±0.030459	3.75918±0.341670	-
65	14.3184±0.000063	0.651397±0.019808	15.1092±0.930873	-
65	11.7912±0.000400	0.333715±0.016031	63.9534±6.601990	-
66	12.7331±0.000335	0.33936±0.009496	95.3831±5.720700	-
66	12.8325±0.000077	0.375504±0.010801	18.3225±0.981380	0.0136187±0.000015
66	13.6887±0.000071	0.628443±0.039339	8.29203±0.961240	-
67	11.2696±0.000302	0.847344±0.018021	111.385±5.115750	-
67	13.9485±0.000946	0.247515±0.017165	110.219±16.092000	-
67	11.4355±0.000462	0.390371±0.020241	65.4771±7.249290	-
67	11.3588±0.000903	0.352731±0.017700	156.9±16.219100	-

Table 1 *continued on next page*

Table 1 (*continued*)

Sol	t_0 (LTST)	ΔP_0 (Pa)	Γ (seconds)	$\max F - \bar{F} /\bar{F}$
67	12.8051±0.000034	0.467988±0.016188	7.36985±0.443763	0.00396651±0.000004
67	12.5359±0.000371	0.443419±0.011595	131.381±6.958530	-
68	14.5098±0.000055	0.423341±0.010217	16.0556±0.813657	-
68	12.9596±0.000209	0.393374±0.010729	54.0982±2.987670	-
68	14.1659±0.000230	0.431733±0.023731	48.2722±4.695430	0.00751445±0.000005
68	14.4107±0.000045	0.781779±0.010930	23.6498±0.698236	-
68	11.3741±0.000459	0.437161±0.010441	228.332±9.477380	-
68	14.1425±0.000024	0.94168±0.023004	7.32391±0.356575	0.00116323±0.093272
68	12.0581±0.000676	0.254082±0.012242	112.301±11.562400	-
68	8.84332±0.000064	0.228421±0.012499	8.42649±0.754644	-
69	13.9638±0.000032	0.91389±0.017011	12.4126±0.488949	-
69	15.1419±0.000059	0.725802±0.046484	6.54069±0.838414	0.00975948±0.000008
69	15.8292±0.000078	0.592243±0.009956	33.6256±1.092790	-
69	13.1258±0.000261	0.461603±0.018095	50.8841±4.297550	-
70	10.42±0.000026	1.02974±0.037422	5.06832±0.386218	-
71	11.6334±0.000109	0.540553±0.020926	19.7646±1.556520	-
71	12.9647±0.000049	0.70821±0.028218	8.74012±0.687636	-
71	14.5197±0.000029	0.868865±0.041632	4.38633±0.369146	-
71	11.9195±0.000219	0.598773±0.019081	49.7158±3.366590	-
71	12.4458±0.000316	0.286955±0.006531	110.1±5.432070	-
71	15.2246±0.000278	0.392417±0.007555	109.84±4.577410	0.0247446±0.000018
72	12.4776±0.000321	0.637639±0.016472	126.675±6.192600	-
72	14.545±0.000264	1.08941±0.058667	37.9096±4.447960	0.00848268±0.000007
72	15.5576±0.000068	0.408489±0.011626	16.0148±0.839815	-
72	12.8114±0.000214	0.325829±0.010170	48.9339±2.942160	0.0031359±0.000007
72	12.4849±0.000161	0.333254±0.019657	40.7476±3.741640	0.0132088±0.000011
72	11.4412±0.000363	0.42745±0.008743	140.9±6.238950	-
72	12.9839±0.000202	0.30551±0.006113	72.2155±2.898750	-
72	11.3478±0.000225	0.262278±0.008604	49.9513±3.456550	-
72	14.0871±0.000257	0.290718±0.007326	77.6242±4.203190	-
73	14.5761±0.000365	0.318566±0.012051	77.5259±6.190330	-
73	13.3221±0.000027	0.745037±0.025481	5.8351±0.373231	0.0149643±0.000015
74	9.91161±0.000124	0.234285±0.016299	12.0704±1.419730	0.00353761±0.000004
74	13.297±0.000035	0.567367±0.049294	2.85043±0.456561	-
74	13.0878±0.000064	0.335911±0.015238	9.99482±0.874881	-
74	13.6628±0.000432	0.321742±0.014464	117.322±8.928660	-
75	12.3853±0.000109	0.409135±0.021665	14.0935±1.462600	0.0172105±0.000017
75	12.0015±0.000876	0.490484±0.037625	217.482±19.913000	0.00477511±0.000012
75	14.5981±0.000308	0.573988±0.009421	140.486±4.983710	-
75	11.1481±0.000046	0.367135±0.009387	12.849±0.632827	-

Table 1 *continued on next page*

Table 1 (*continued*)

Sol	t_0 (LTST)	ΔP_0 (Pa)	Γ (seconds)	$\max F - \bar{F} /\bar{F}$
76	10.4208±0.000018	0.741544±0.011883	8.06991±0.270876	-
76	14.2839±0.000187	0.361483±0.014327	36.6803±3.133330	-
76	11.8897±0.000196	0.414155±0.011393	50.3771±2.684360	-
76	10.7817±0.000035	0.634844±0.060987	2.0±0.332294	-
76	14.2047±0.000226	0.299691±0.027964	17.5257±3.053250	-
77	13.6868±0.000170	0.531214±0.014571	46.8866±2.767430	0.034374±0.000008
77	11.6055±0.000252	0.486585±0.018059	71.3924±4.929000	0.00369892±0.000007
77	13.2979±0.000195	0.252544±0.023568	14.9024±2.821540	0.00584893±0.000007
78	10.7192±0.000075	0.410513±0.013171	17.0257±1.137860	-
78	14.8294±0.000366	0.410087±0.008782	126.305±5.832240	0.0099874±0.000007
78	12.5989±0.000062	0.556009±0.012738	20.9994±1.038190	-
78	12.0035±0.000111	1.88952±0.115853	13.5289±1.769460	0.0181365±0.000023
79	10.9165±0.000032	0.610542±0.014011	10.0608±0.467177	-
79	13.7891±0.000321	0.363553±0.009670	87.9592±4.970160	-
79	12.8566±0.000047	0.697316±0.021539	10.7705±0.666190	0.015443±0.000008
79	11.7686±0.000174	0.376947±0.027161	20.077±2.977000	-
80	12.0939±0.000414	0.357339±0.023467	45.5239±6.053550	-
80	12.5141±0.000081	0.338876±0.010060	19.2035±1.190290	-
80	12.8021±0.000334	0.382872±0.008718	105.321±4.952740	-
80	16.0765±0.000041	0.66429±0.015716	12.4528±0.618716	-
80	14.7499±0.000053	1.58486±0.124890	4.78081±0.777090	-
81	14.8984±0.000022	0.551505±0.056916	2.00083±0.340868	-
81	11.5329±0.000038	0.53946±0.014032	10.3113±0.527211	-
81	11.7642±0.000074	0.563391±0.023778	12.9626±1.176670	0.00480811±0.000007
81	12.9375±0.000015	1.38056±0.023629	6.23106±0.219409	0.0343043±0.000006
81	9.89857±0.000035	0.401879±0.014123	6.97557±0.472609	-
82	12.0778±0.000160	5.73019±0.936916	7.20716±2.428300	-
82	10.6237±0.000031	0.715905±0.056560	2.95458±0.403493	-
82	14.7231±0.000063	0.333155±0.015379	9.62392±0.871898	-
83	11.3286±0.000036	0.588705±0.013813	11.2365±0.549016	0.009447±0.000006
83	11.9107±0.000047	0.874197±0.048218	6.1718±0.687888	0.0199629±0.000017
83	11.9307±0.000019	0.749664±0.017992	5.75269±0.289342	-
83	14.8521±0.000558	0.238797±0.010837	91.7175±9.019900	-
84	15.8881±0.000029	0.661909±0.025413	5.38251±0.421922	0.00610052±0.000092
84	12.5604±0.000187	0.439091±0.020068	31.8827±3.184810	-
85	11.7397±0.000089	1.61588±0.038904	28.4457±1.472920	0.0211287±0.000034
85	15.5834±0.000042	2.29611±0.199454	3.41202±0.570201	0.0183279±0.000079
85	11.8839±0.000113	0.462945±0.019936	19.0398±1.448220	6.0075e-06±0.000002
85	15.395±0.000098	0.440499±0.019357	16.1574±1.424250	-
85	11.3939±0.000234	0.32012±0.016546	32.8135±2.885290	-

Table 1 *continued on next page*

Table 1 (*continued*)

Sol	t_0 (LTST)	ΔP_0 (Pa)	Γ (seconds)	$\max F - \bar{F} /\bar{F}$
85	13.7222 \pm 0.000256	0.415608 \pm 0.010617	84.201 \pm 4.559480	-
85	13.9305 \pm 0.000041	0.580076 \pm 0.018800	9.01362 \pm 0.582059	0.00759514 \pm 0.000009
86	14.3959 \pm 0.000058	0.429443 \pm 0.012952	13.6775 \pm 0.774281	-
86	12.5671 \pm 0.000010	0.605617 \pm 0.010313	4.13718 \pm 0.133809	-
86	12.0357 \pm 0.000121	0.696343 \pm 0.011765	57.924 \pm 2.095520	-
86	10.6706 \pm 0.000016	0.53129 \pm 0.012850	4.77083 \pm 0.245408	-
87	13.0463 \pm 0.000120	0.726998 \pm 0.018061	35.2643 \pm 1.902690	-
87	13.3126 \pm 0.000142	0.326179 \pm 0.006202	52.5493 \pm 2.023150	-
87	13.1986 \pm 0.000362	0.31096 \pm 0.017302	46.2664 \pm 4.549570	-
87	13.8564 \pm 0.000363	0.623663 \pm 0.013625	140.593 \pm 6.457290	-
88	12.0712 \pm 0.000038	0.904238 \pm 0.022322	11.223 \pm 0.552735	0.0227441 \pm 0.000029
89	13.4568 \pm 0.000953	0.364189 \pm 0.013778	202.229 \pm 16.241300	-
89	13.913 \pm 0.000043	0.539182 \pm 0.019906	8.33823 \pm 0.655382	-
89	14.9657 \pm 0.000009	2.65486 \pm 0.046108	3.52944 \pm 0.121967	-
89	11.3571 \pm 0.000059	1.40755 \pm 0.028278	21.5007 \pm 0.924961	-

NOTE—The full table is also available at https://github.com/BoiseStatePlanetary/Vortices-and-Dust-Devils-As-Observed-by-Mars-2020/blob/main/figures/vortex_params.csv. For encounters without statistically meaningful RDS excursions, $\max|F - \bar{F}|/\bar{F}$ is not given.

Figure 3 illustrates the resulting best-fit ΔP_0 - and Γ -values for the collection of 309 recovered vortex signals that we retained throughout this study, and Table 1 provides an abbreviated list of the values. (After applying the matched filter and model-fitting analysis described above, we discarded 22 putative vortex signals with apparent $\Gamma > 250$ s and $\Delta P_0/\sigma_{\Delta P} < 5$, which consistently seemed to be either spurious detections or spikes resulting from the edge effects from our detrending process.)

As in previous studies (e.g., Lorenz et al. 2021), we fit power-laws to the cumulative histogram of ΔP_0 -values. As discussed next, assessing our ability to recover synthetic vortices with known ΔP_0 - and Γ -values indicates we could consistently recover vortices with $\Delta P_0 \gtrsim 0.6$ Pa (111 vortices), and so we used the Levenberg-Marquardt algorithm to fit the power-laws using only those deeper vortices. Poisson sampling was assumed to estimate bin uncertainties. The cumulative histogram shows an apparent knee at about $\Delta P_0 = 1.5$ Pa, so we also fit a power-law to these vortices, although this result is likely skewed by small number statistics (we found only 19 such vortices).

In order to assess the robustness of our detection scheme, we conducted several injection-recovery experiments for which we injected vortex signals with known parameters into the raw pressure time-series and then applied our scheme to determine how often we could successfully recover the vortices. Figure 4 shows the results for the sol with a time-series exhibiting the largest scatter, sol 82. We find that we can consistently recover signals with $\Delta P_0 = 0.6$ Pa but that the scatter often obscures less deep signals. Thus in our power-law analysis, we focused on the deeper vortex signals.

Our results here are roughly consistent with recent analyses of data from the InSight mission. Analyzing data from the mission’s pressure sensor APSS, Spiga et al. (2021) reported a power-law index for vortex detections with $0.35 \text{ Pa} \leq \Delta P_0 \leq 9 \text{ Pa}$ consistent with -2.4 ± 0.3 for the cumulative histogram. Lorenz et al. (2021) conducted an analysis of the same dataset and, considering vortices with $0.8 \text{ Pa} < \Delta P_0 < 3 \text{ Pa}$, found a power-law index of -2 . For deeper vortices, an index of -3 was suggested to provide a better fit. Jackson et al. (2021) reported an overall index of -2.39 ± 0.02 for vortices with $\Delta P_0 > 1 \text{ Pa}$.

We can also explore the vortex encounter rate for Perseverance. Figure 5 show the encounters binned by sol as blue bars. As indicated above, several sols have no data available, and others have data problematic for our study, as

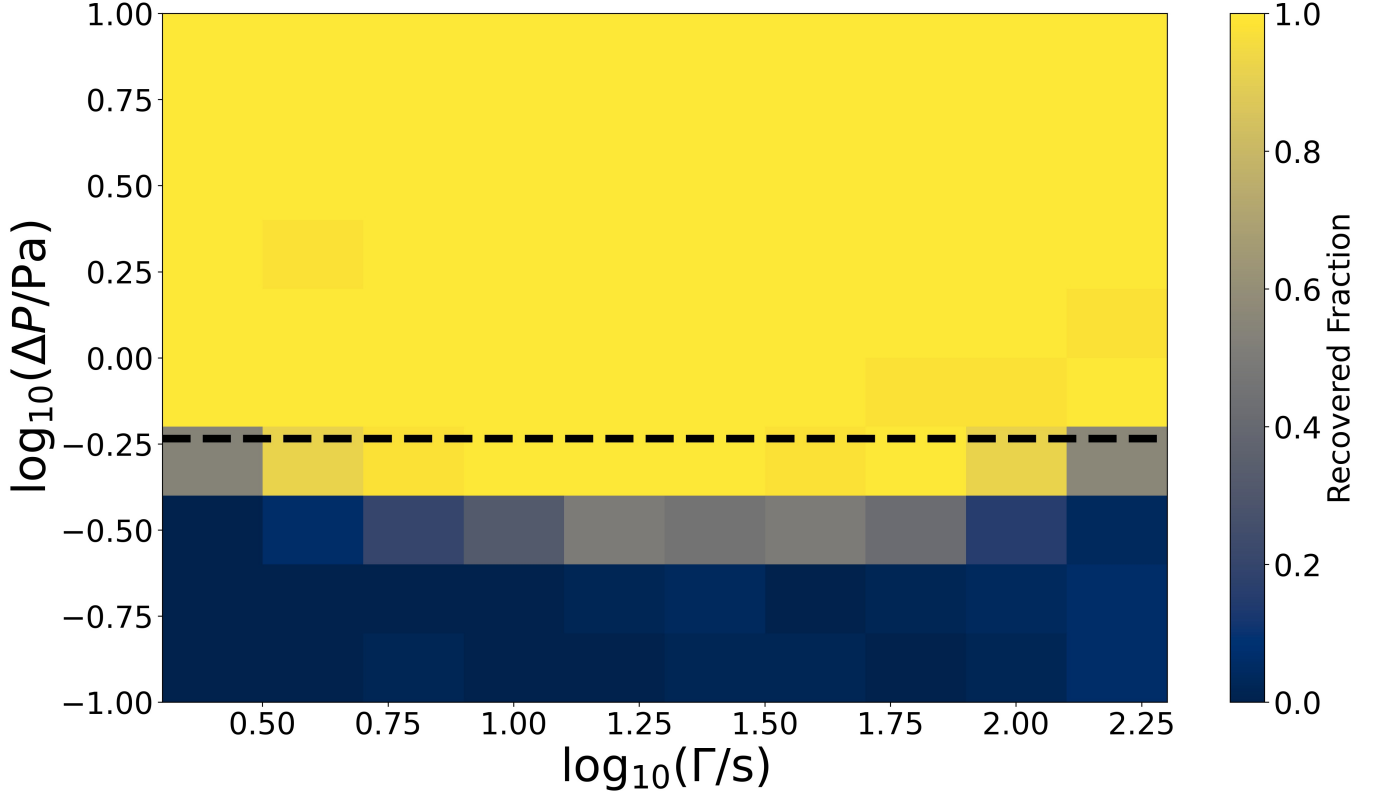


Figure 4. Results from an injection-recovery calculation using data from the sol with the largest scatter in ΔP (0.08 Pa), sol 82. The dashed black line shows the detection threshold, which corresponds to $\Delta P_0 = 0.6$ Pa. All but the very shortest or longest duration vortices with ΔP_0 above that threshold are consistently recovered.

indicated in the figure. For the 65 sols with available, usable data, there was an average rate of 4.75 encounters per sol, with variations between 0 and 10. Some sols had more data available than others, however. To account for that variation (between 7 and 17 hours of observations from sol to sol), we divided the number of encounters on a given sol by the total number of hours (or fractions thereof) of observational data, giving the orange bars in Figure 5. We can then see that the typical sol saw an encounter about every three hours (at least while data were collected), up to a maximum of one every 43 minutes (1.4 encounters per hour).

The encounter rates also show hour-to-hour variation, as illustrated by the blue bars in Figure 6. As in Figure 5, we have normalized the number of encounters during each hour by the total number of hours (over all available/usable sols) to estimate the hourly encounter rate. As seen in previous studies (e.g., Jackson et al. 2021), the encounter rate peaks about mid-day, in this case at 1.5 encounters per hour (once every 40 minutes), dropping below detectable levels early in the morning and late in the afternoon; however, encounters persist until 19:00 LTST.

3.1. Are vortices at Jezero Crater more active than at the landing sites of other recent missions?

These results corroborate predictions that vortex activity at Jezero would exceed activity at Gale Crater, the exploration site for the Mars Science Laboratory rover (MSL) Curiosity, and likely at the landing site for the InSight mission. The comprehensive results in Newman et al. (2021) predicted significantly elevated vortex activity based on the high values estimated for the “dust devil activity” DDA. This parameter combines a measure of the thermodynamic efficiency of dust devil convection with the near-surface sensible heat flux, two parameters thought key for vortex activity (Rennó et al. 1998). How exactly this parameter maps to vortex occurrence (Does larger DDA mean more vortices overall? More vigorous vortices? etc.) remains unclear, but DDA is a metric derivable from general circulation models and large eddy simulations and likely has some bearing on vortex occurrence. Thus, a fuller understanding of its relationship to vortex properties would elucidate key boundary layer processes.

Newman et al. (2019) analyzed three Mars years of pressure and wind time-series from Curiosity, spanning sols 1 to 1980 of the mission, and estimated vortex encounter rates that varied from sol to sol, season to season. Considering

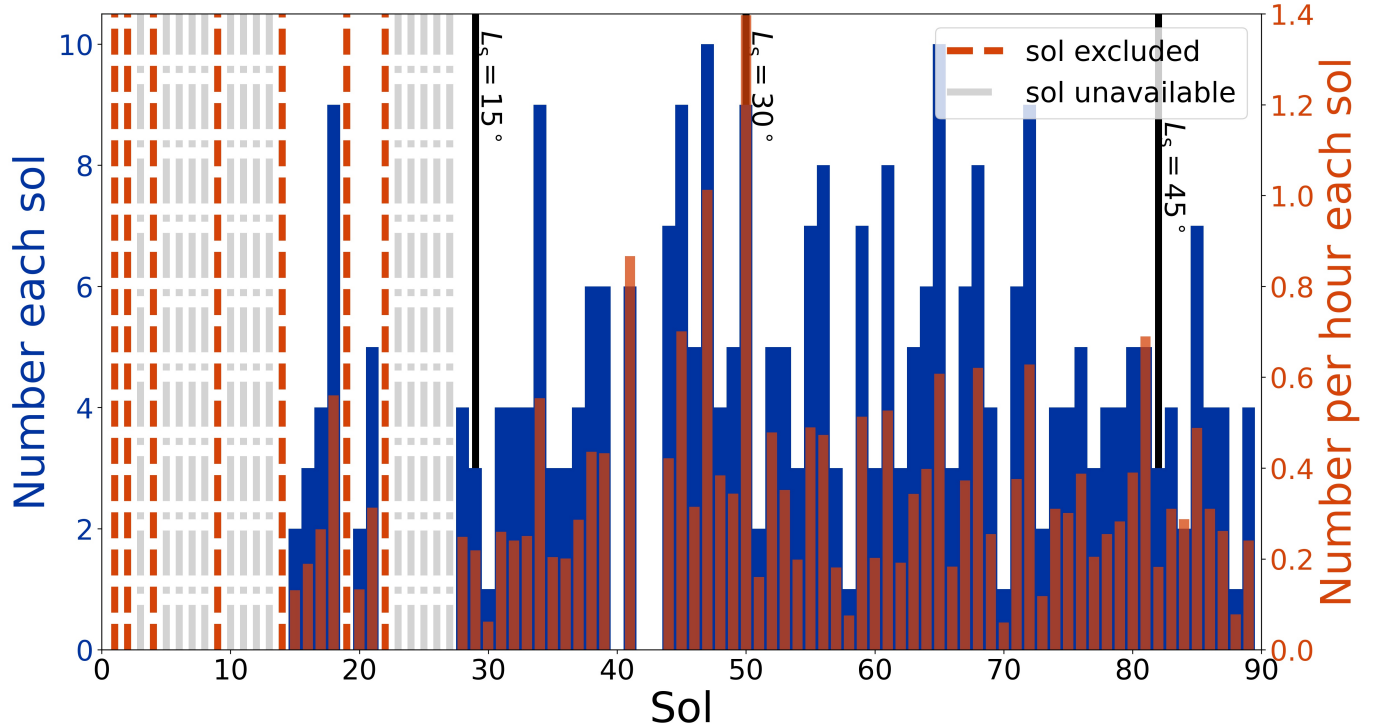


Figure 5. The blue bars show the number of vortex encounters during each sol, while the orange bars show the number of encounters each sol divided by the total number hours during which the pressure sensor collected data. The dashed orange lines show sols when pressure data were available but were flawed or inadequate and so excluded for our analysis. The grey dash-dotted lines show sols when data were unavailable. Solid black lines indicate L_s -values.

pressure excursions greater than 0.6 Pa, that study reported hourly encounter rates that topped out at about 1 per hour but was more typically 0.5 per hour (when it was not zero). Per-sol encounter rates topped out at about 4 per sol (during the summer), with a typical non-zero value of 1 per sol. [Ordóñez-Etxeberria et al. \(2018\)](#) conducted a similar survey of the first two Mars years of pressure data from Curiosity and found similar encounter rates for pressure excursions exceeding 0.5 Pa. Comparing to the results in Figure 5 and 6, it seems clear that Perseverance saw more vortices with similar minimum pressure excursions.

With regard to the InSight results, there appears to be some mismatch between different studies. [Spiga et al. \(2021\)](#) analyzed the first 400 sols of InSight pressure time-series data and reported more than 6000 vortex encounters with pressure excursions exceeding 0.35 Pa. Considering only encounters with an excursion exceeding 0.5 Pa, they reported an overall encounter rate of 7 per sol, with (non-zero) rates varying between 1 and 17 per sol. [Lorenz et al. \(2021\)](#) also sifted the InSight pressure and wind data for vortex encounters. Considering a minimum excursion of 0.8 Pa, that study reported an overall rate of 2-3 encounters per sol, which, using the results of the histogram analyses from that study (their Figure 4), works out to about 5 encounters per sol for an excursion greater than 0.5 Pa. [Jackson et al. \(2021\)](#) conducted an independent analysis of a slightly enlarged InSight dataset (477 sols worth) and found encounter rates topping out at 3 per sol and 0.4 per hour for excursions exceeding 0.3 Pa. [Jackson et al. \(2021\)](#) discussed possible reasons for the mismatches between these studies. In any case, the per-sol encounter rates reported here for Perseverance (Figures 5) often match or exceed all but the highest rates reported in those previous studies. ([Spiga et al. 2021](#) and [Lorenz et al. 2021](#) do not report per-hour encounter rates.)

The fractional area covered by dust devils has been cited as a useful metric for estimating the likelihood of vortex encounters for a landed spacecraft. [Lorenz et al. \(2021\)](#) pointed out that the fractional area can be estimated by comparing the total durations of all vortex encounters to the total observational time. The total duration of encounters is about 3.56 hours, while the total observational time over the 89 sols is about 966 hours. Together, these numbers suggest a fractional area of 0.367%, about five times larger than the fractional area seen for vortices at InSight ([Lorenz et al. 2021](#); [Jackson et al. 2021](#)).

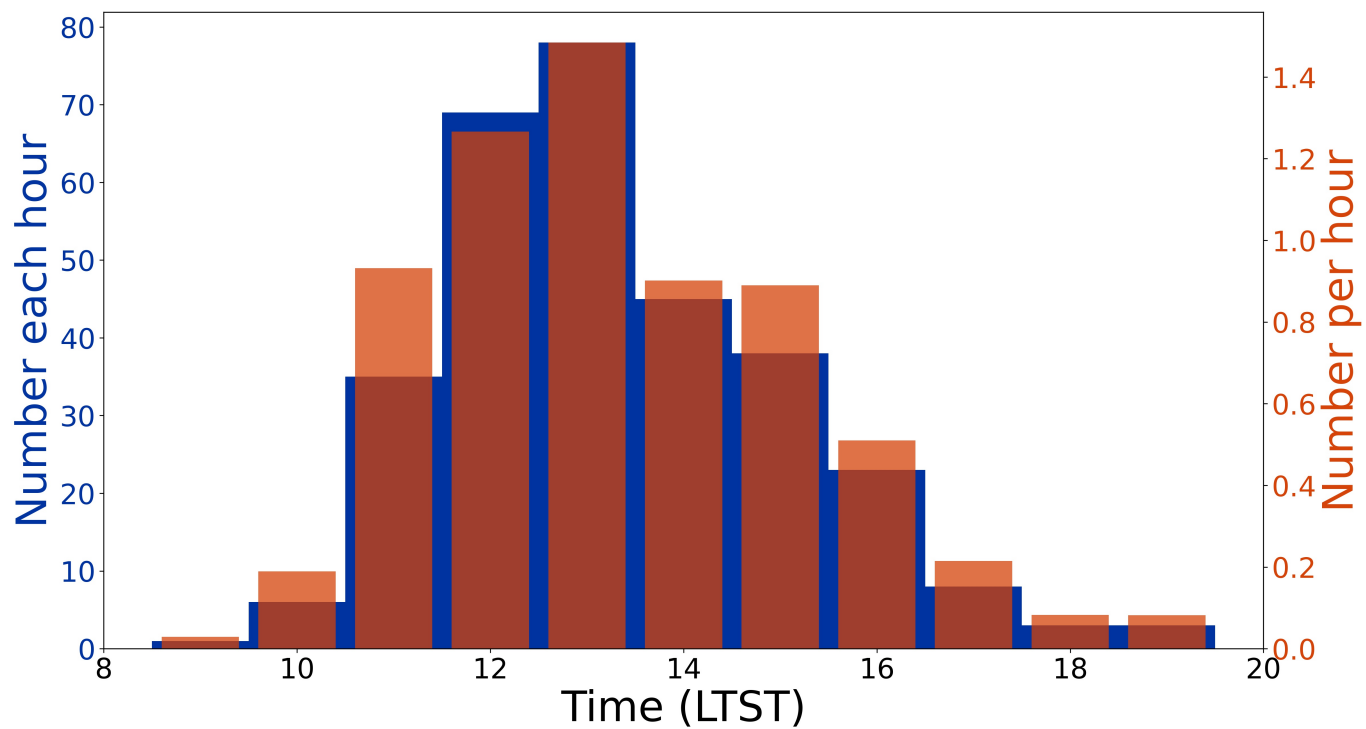


Figure 6. The blue bars show the total number of vortex encounters that took place during that hour over the whole 89 sol dataset, while the orange bars show that number divided by the total number of hours during that period each sol observed throughout the 89 sol dataset.

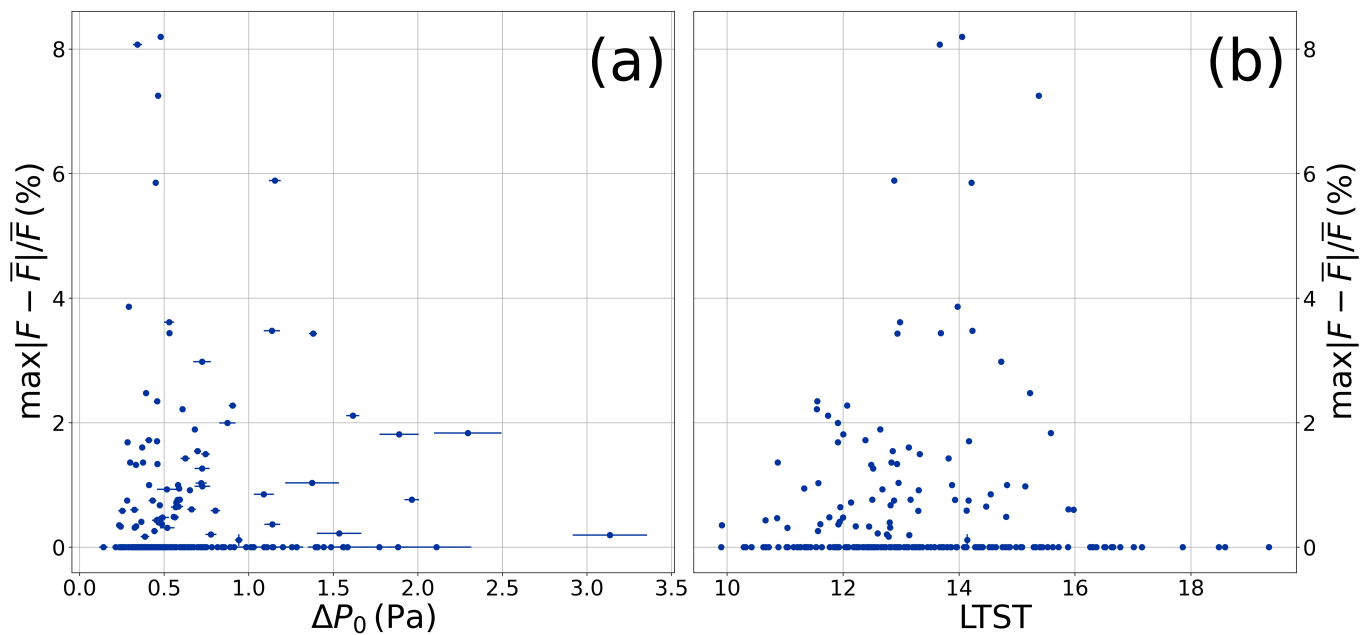


Figure 7. (a) RDS excursions vs. the observed ΔP_0 -value for the vortex encounters. (b) RDS excursions vs. the time-of-sol for the encounter. Error bars for all estimated variables are shown but are smaller than the plot symbol in most cases.

3.2. What fraction of encountered vortices are true dust devils?

Figure 7 provides some insight into how often vortices are dusty. As previously indicated, about one-third (91 of our total 309) produced a discernible radiative signal. At face value, this result suggests about one third of the encountered vortices lofted dust at the level it could be detected. This fraction compares favorably to results from [Lorenz & Jackson \(2015\)](#). That study involved a terrestrial deployment of pressure loggers and solar insolation sensors and found that about 20% of vortex encounters exhibited insolation excursions of 2% or greater (a 30% excursion in one case). Of course, the actual geometry of the encounter dictates whether a dust vortex will produce an excursion (Does the vortex pass on the sunward or anti-sunward side of the sensor?), but there is no obvious reason for the encounter geometries from [Lorenz & Jackson \(2015\)](#) to differ substantially from the geometries for Perseverance, at least not at first order.

The fraction of apparently dusty vortices reported here also closely matches the maximum fraction inferred in [Jackson et al. \(2021\)](#). As in [Spiga et al. \(2021\)](#), that study reported no visual detections of dust devils, and the InSight lander does not include any insolation sensors. However, [Jackson et al. \(2021\)](#) used the lack of imaged dust devils, convolved with the frequency of imaging and of vortex encounters, to infer an upper limit for the fraction of vortices lofting measurable amounts of dust at 35%.

The conditions that allow a vortex to loft dust remain obscure, in spite of decades of field studies, laboratory experiments, and modeling ([Rafkin et al. 2016](#)). However, the results here can help shed some light. Among vortices with measurable radiative excursions in Figure 7, the encounter with the smallest excursion that is also more than $5\text{-}\sigma_F$ greater than zero (meaning the excursion is credibly non-zero) is $\max|F - \bar{F}|/\bar{F} = 0.0017 \pm 5 \times 10^{-6}$ and has $\Delta P_0 = 0.39 \text{ Pa}$. Assuming cyclostrophic balance ([Kurgansky et al. 2016](#)), this pressure deficit corresponds to an eyewall velocity of about 4 m s^{-1} ($= \sqrt{0.39 \text{ Pa}/0.02 \text{ kg m}^{-2}}$), well below the expected threshold for dust-lifting on Mars, between 20 and 30 m s^{-1} ([Greeley et al. 2003](#)). An eyewall velocity of 20 m s^{-1} corresponds to a central pressure dip for a vortex of $\Delta P = 8 \text{ Pa}$ ($= (20 \text{ m s}^{-1})^2 \times (0.02 \text{ kg m}^{-3})$). We can see from Figure 7 that none of our encounters registered such a large pressure excursion. These results suggest that, if 20 m s^{-1} is the true lifting threshold, all of our apparently dusty vortices were encountered off-center, giving observed pressure minimum ΔP_0 well below the central values, as expected statistically ([Jackson et al. 2018](#); [Kurgansky 2019](#)).

The dusty vortex with the deepest pressure signal ($\Delta P_0 = 3.1 \text{ Pa}$) also has one of the smallest radiative excursions. Indeed, there is a dearth of vortex encounters with large ΔP_0 and large radiative excursions in Figure 7(a), which seems counter-intuitive: we might expect the most vigorous vortices to lift the most dust. Theoretical expectations ([Jackson 2020](#)) and observations of martian dust devils ([Greeley et al. 2006](#)) corroborate this expectation. Instead, this dearth may arise simply from the vortex encounter geometries. A relatively low pressure (small ΔP_0) signal may result either from a (more likely) distant encounter with a vigorous (large central pressure deficit) and very dusty vortex *or* from a nearby encounter with a weak (small central pressure deficit) and low-dust vortex. The former encounter may result in a large RDS excursion, the latter in a small excursion. The spread in RDS excursions for the smallest ΔP_0 -values in Figure 7 appears to corroborate that expectation. By contrast, a relatively high pressure signal (large ΔP_0) is most likely to result from a nearly central encounter. During such an encounter, the Sun will only be occulted by one wall of the dust devil, resulting in a relatively low optical depth encounter. In any case, the completely processed wind data from MEDA (when available) will be crucial for understanding these trends since the wind speed and/or direction measurements may allow independent determination of the encounter geometry ([Lorenz 2016](#); [Kahanpää & Viúdez-Moreiras 2021](#); [Jackson et al. 2021](#)).

Figure 7(b) reveals a pattern easier to interpret. The largest RDS excursions occur at very nearly the same time of day as the peak in occurrence rate. Since DDA also peaks near 13:00 LTST ([Newman et al. 2021](#)), these results seem to suggest that larger values of DDA correspond both to increased vortex encounter rates and enhanced dust lofting. DDA increases, in part, with as the boundary layer deepens, which likely results in taller dust devils. [Jackson \(2020\)](#) suggested that taller dust devils ought to have larger dust densities, and the results here comport with that prediction.

4. CONCLUSIONS

This study presents a preliminary analysis of vortex and dust devil encounters from the first 89 sols of data from the Perseverance rover’s MEDA meteorological suite. Although some key data are not yet completely processed or available, including the wind measurements, we can draw some tentative but intriguing conclusions. The distribution of observed pressure excursions for the vortex encounters satisfies a power-law fit in agreement with other analyses (cf. [Lorenz & Jackson 2016](#)). The hour-by-hour encounter rate varies throughout the sol with a peak near mid-day,

again, similar to previous observational studies (Murphy et al. 2016) and model predictions tailored to Jezero Crater (Newman et al. 2021).

Our results suggest vortex encounters for Perseverance exceed the encounter rates at Curiosity by between a factor of 5 to 10. The rates likely exceed those at InSight, but there is some disagreement about InSight’s precise encounter rate between previous studies. Perseverance’s RDS instrument allows us to assess whether a vortex was actually dust-laden as dusty vortices induced positive and negative excursions in the RDS time-series as a result of light-scattering. One-third of the vortices show signs of dust-lofting.

As additional data are made available and processed from Perseverance, additional insights can be gleaned. Auspiciously, Newman et al. (2021) actually predict higher DDA-values for the summer season, so we might expect even higher vortex encounter rates than reported here. A complete model accounting for temporally and spatially evolving phase angles, complex light-scattering properties of the dust, etc. (e.g., Mason et al. 2013) could return a robust assessment of dust profiles from the RDS time-series. Estimates of the durations of the RDS signals may provide dust devil diameters. Analysis of the wind speed and directional data can also elucidate vortex diameters and even encounter geometries. A detailed survey of imagery from the engineering cameras and Mastcam-Z can constrain dust devil frequency, diameters, and dustiness (Greeley et al. 2010).

This study benefited from conversations with Ryan Battin, Justin Crevier, Lori Fenton, Ralph Lorenz, and Michelle Szurgot. This research was supported by a grant from NASA’s Solar System Workings program, NNH17ZDA001N-SSW.

Software: matplotlib (Hunter 2007), numpy (Harris et al. 2020), scipy (Virtanen et al. 2020), Astropy (Astropy Collaboration et al. 2013, 2018)

REFERENCES

- Astropy Collaboration, Robitaille, T. P., Tollerud, E. J., et al. 2013, *A&A*, 558, A33, doi: [10.1051/0004-6361/201322068](https://doi.org/10.1051/0004-6361/201322068)
- Astropy Collaboration, Price-Whelan, A. M., Sipőcz, B. M., et al. 2018, *AJ*, 156, 123, doi: [10.3847/1538-3881/aabc4f](https://doi.org/10.3847/1538-3881/aabc4f)
- Basu, S., Richardson, M. I., & Wilson, R. J. 2004, *Journal of Geophysical Research (Planets)*, 109, E11006, doi: [10.1029/2004JE002243](https://doi.org/10.1029/2004JE002243)
- Farley, K. A., Williford, K. H., Stack, K. M., et al. 2020, *SSRv*, 216, 142, doi: [10.1007/s11214-020-00762-y](https://doi.org/10.1007/s11214-020-00762-y)
- Fenton, L., Reiss, D., Lemmon, M., et al. 2016, *SSRv*, 203, 89, doi: [10.1007/s11214-016-0243-6](https://doi.org/10.1007/s11214-016-0243-6)
- Fenton, L. K., & Lorenz, R. 2015, *Icarus*, 260, 246, doi: [10.1016/j.icarus.2015.07.028](https://doi.org/10.1016/j.icarus.2015.07.028)
- Greeley, R., Balme, M. R., Iversen, J. D., et al. 2003, *Journal of Geophysical Research (Planets)*, 108, 5041, doi: [10.1029/2002JE001987](https://doi.org/10.1029/2002JE001987)
- Greeley, R., Whelley, P. L., Arvidson, R. E., et al. 2006, *Journal of Geophysical Research (Planets)*, 111, E12S09, doi: [10.1029/2006JE002743](https://doi.org/10.1029/2006JE002743)
- Greeley, R., Waller, D. A., Cabrol, N. A., et al. 2010, *Journal of Geophysical Research (Planets)*, 115, E00F02, doi: [10.1029/2010JE003608](https://doi.org/10.1029/2010JE003608)
- Harris, C. R., Millman, K. J., van der Walt, S. J., et al. 2020, *Nature*, 585, 357, doi: [10.1038/s41586-020-2649-2](https://doi.org/10.1038/s41586-020-2649-2)
- Hunter, J. D. 2007, *Computing in Science & Engineering*, 9, 90, doi: [10.1109/MCSE.2007.55](https://doi.org/10.1109/MCSE.2007.55)
- Jackson, B. 2020, *Icarus*, 338, 113523, doi: [10.1016/j.icarus.2019.113523](https://doi.org/10.1016/j.icarus.2019.113523)
- Jackson, B., Crevier, J., Szurgot, M., et al. 2021, arXiv e-prints, arXiv:2107.12456, <https://arxiv.org/abs/2107.12456>
- Jackson, B., Lorenz, R., & Davis, K. 2018, *Icarus*, 299, 166, doi: [10.1016/j.icarus.2017.07.027](https://doi.org/10.1016/j.icarus.2017.07.027)
- Kahanpää, H., & Viúdez-Moreiras, D. 2021, *Icarus*, 359, 114207, doi: [10.1016/j.icarus.2020.114207](https://doi.org/10.1016/j.icarus.2020.114207)
- Kurgansky, M. V. 2019, *Icarus*, 317, 209, doi: [10.1016/j.icarus.2018.08.004](https://doi.org/10.1016/j.icarus.2018.08.004)
- Kurgansky, M. V., Lorenz, R. D., Renno, N. O., et al. 2016, *SSRv*, 203, 209, doi: [10.1007/s11214-016-0281-0](https://doi.org/10.1007/s11214-016-0281-0)
- Lorenz, R. D. 2016, *Icarus*, 271, 326, doi: [10.1016/j.icarus.2016.02.001](https://doi.org/10.1016/j.icarus.2016.02.001)
- Lorenz, R. D., & Jackson, B. K. 2015, *GeoResJ*, 5, 1, doi: <https://doi.org/10.1016/j.grj.2014.11.002>
- Lorenz, R. D., & Jackson, B. K. 2016, *SSRv*, 203, 277, doi: [10.1007/s11214-016-0277-9](https://doi.org/10.1007/s11214-016-0277-9)
- Lorenz, R. D., Spiga, A., Lognonné, P., et al. 2021, *Icarus*, 355, 114119, doi: [10.1016/j.icarus.2020.114119](https://doi.org/10.1016/j.icarus.2020.114119)
- Mason, J. P., Patel, M. R., & Lewis, S. R. 2013, *Icarus*, 223, 1, doi: [10.1016/j.icarus.2012.11.018](https://doi.org/10.1016/j.icarus.2012.11.018)

- Murphy, J., Steakley, K., Balme, M., et al. 2016, SSRv, 203, 39, doi: [10.1007/s11214-016-0283-y](https://doi.org/10.1007/s11214-016-0283-y)
- Newman, C. E., Kahanpää, H., Richardson, M. I., et al. 2019, Journal of Geophysical Research (Planets), 124, 3442, doi: [10.1029/2019JE006082](https://doi.org/10.1029/2019JE006082)
- Newman, C. E., de la Torre Juárez, M., Pla-García, J., et al. 2021, SSRv, 217, 20, doi: [10.1007/s11214-020-00788-2](https://doi.org/10.1007/s11214-020-00788-2)
- Ordóñez-Etxeberria, I., Hueso, R., & Sánchez-Lavega, A. 2018, Icarus, 299, 308, doi: [10.1016/j.icarus.2017.07.032](https://doi.org/10.1016/j.icarus.2017.07.032)
- Pla-García, J., Rafkin, S. C. R., Martínez, G. M., et al. 2020, SSRv, 216, 148, doi: [10.1007/s11214-020-00763-x](https://doi.org/10.1007/s11214-020-00763-x)
- Press, W. H., Teukolsky, S. A., Vetterling, W. T., & Flannery, B. P. 2007, Numerical Recipes 3rd Edition: The Art of Scientific Computing, 3rd edn. (Cambridge University Press). http://www.amazon.com/Numerical-Recipes-3rd-Scientific-Computing/dp/0521880688/ref=sr_1_1?ie=UTF8&s=books&qid=1280322496&sr=8-1
- Rafkin, S., Jemmett-Smith, B., Fenton, L., et al. 2016, SSRv, 203, 183, doi: [10.1007/s11214-016-0307-7](https://doi.org/10.1007/s11214-016-0307-7)
- Rennó, N. O., Burkett, M. L., & Larkin, M. P. 1998, Journal of Atmospheric Sciences, 55, 3244, doi: [10.1175/1520-0469\(1998\)055<3244:ASTTFD>2.0.CO;2](https://doi.org/10.1175/1520-0469(1998)055<3244:ASTTFD>2.0.CO;2)
- Ringrose, T. J., Towner, M. C., & Zarnecki, J. C. 2003, Icarus, 163, 78, doi: [10.1016/S0019-1035\(03\)00073-3](https://doi.org/10.1016/S0019-1035(03)00073-3)
- Rodríguez-Manfredi, J. A., de la Torre Juárez, M., Alonso, A., et al. 2021, SSRv, 217, 48, doi: [10.1007/s11214-021-00816-9](https://doi.org/10.1007/s11214-021-00816-9)
- Spiga, A., Murdoch, N., Lorenz, R., et al. 2021, Journal of Geophysical Research (Planets), 126, e06511, doi: [10.1029/2020JE006511](https://doi.org/10.1029/2020JE006511)
- Steakley, K., & Murphy, J. 2016, Icarus, 278, 180, doi: [10.1016/j.icarus.2016.06.010](https://doi.org/10.1016/j.icarus.2016.06.010)
- Thomas, P., & Gierasch, P. J. 1985, Science, 230, 175, doi: [10.1126/science.230.4722.175](https://doi.org/10.1126/science.230.4722.175)
- Virtanen, P., Gommers, R., Oliphant, T. E., et al. 2020, Nature Methods, 17, 261, doi: [10.1038/s41592-019-0686-2](https://doi.org/10.1038/s41592-019-0686-2)